University of Groningen

Multiwavelength study of the star-formation in the bar of NGC 2903

Popping, G.; Perez, I.; Zurita, A.

IMPORTANT NOTE: You are advised to consult the publisher's version (publisher's PDF) if you wish to cite from it. Please check the document version below.

Document Version
Publisher's PDF, also known as Version of record

Publication date:
2010

[Link to publication in University of Groningen/UMCG research database](#)

Astronomy
&
Astrophysics

Multiwavelength study of the star-formation in the bar of NGC 2903

G. Popping[1], I. Pérez[2,3], and A. Zurita[2,3]

[1] Kapteyn Astronomical Institute, PO Box 800, 9700 AV Groningen, The Netherlands
e-mail: G.Popping@astro.rug.nl
[2] Dep. Física Teórica y del Cosmos, Campus de Fuentenueva, Universidad de Granada, 18071 Granada, Spain
[3] Instituto Carlos I de Física Teórica y Computación, Spain

ABSTRACT

Aims. The nearby barred spiral NGC 2903 has an active starburst at its centre and H II regions distributed along its bar. We analyse the star-formation properties in the bar region of NGC 2903 and study its links to the typical bar morphological features.
Methods. We combine space and ground-based data from the far-ultraviolet to the sub-millimeter spectral ranges to create a panchromatic view of the NGC 2903 bar. We produce two catalogues: one for the current star-formation regions, as traced by the Hα compact emission, and a second for the ultraviolet (UV) emitting knots, containing positions and luminosities. From them, we obtain ultraviolet colours, star-formation rates, dust attenuation, and Hα *EW*s, and analyse their spatial distribution. We estimate stellar cluster ages using stellar population synthesis models (*Starburst99*).
Results. We find NGC 2903 to be a complex galaxy that has a very different morphology in each spectral band. The CO ($J = 1-0$) and the 3.6 μm emission trace each other in a clear barred structure, while the Hα leads both components and has an s-shape distribution. The UV emission is patchy and does not resemble a bar. The UV emission is also characterised by a number of regions located symmetrically with respect to the galaxy centre, almost perpendicular to the bar, in a spiral shape covering the inner ~2.5 kpc. These regions exhibit a significant amount of neither Hα nor 24 μm emission. We estimate ages for these regions ranging from 150 to 320 Myr, older than the remaining UV knots, which have ages lower than 10 Myr. The SFR calculated from the UV emission is ~0.4 $M_{\odot}$ yr^{-1}, compatible with the SFR derived from Hα calibrations (~1 $M_{\odot}$ yr^{-1}).

Key words. galaxies: star formation – galaxies: structure – galaxies: individual: NGC 2903 – galaxies: evolution – HII regions – ultraviolet: galaxies

1. Introduction

Following the launch of both the *Spitzer* Space Telescope and the GALaxy Evolution eXplorer (*GALEX*), knowledge about the star-formation (SF) in galaxies has grown considerably. The panchromatic view of nearby galaxies offered by large surveys carried out by these space telescope missions have provided extraordinary databases with which to study star-formation in galaxies. In particular, it has allowed us to link general galaxy properties to those of the local interstellar medium (ISM) properties and the galaxy dynamics. Identifying these links is crucial for understanding SF in galaxies. In nearby galaxies, these sets of multiwavelength data provide an opportunity to study in detail, with good spatial resolution, the location and properties of relatively young populations, recent massive star-formation, and dust attenuation (e.g.; Calzetti et al. 2005; Tamura et al. 2009; Relaño & Kennicutt 2009).

New dust and SF indicators have been developed and calibrated using all the available bands. The combination of 24 μm and Hα emission has become a reliable indicator of dust attenuation (Kennicutt et al. 2007; Relaño & Kennicutt 2009). Both bands are linked to star-formation processes, with the Hα emission originating from the recombination of hydrogen in the surrounding medium of very recently formed (less than a few Myr) massive stars, and the 24 μm emission tracing ionising radiation from young stars obscured by dust (Calzetti et al. 2005). Extinction-corrected UV emission can also be used to retrieve the star-formation rate (SFR) (Kennicutt 1998) and to obtain some insight into the star-formation that has occurred in the past Gyr (e.g.; Bianchi et al. 2005; Hibbard et al. 2005). A combination of UV, Hα, and 24 μm emission is indeed ideal for reconstructing the recent star-formation history of a galaxy by studying the location and properties of individual clusters and those of the gas and dust emission around them. To date, and to our knowledge, only a few galaxies have been analysed in this way; M 51 (Calzetti et al. 2005), M 81 (Pérez-González et al. 2006), M 33 (Relaño & Kennicutt 2009; Verley et al. 2009), and NGC 7331 (Thilker et al. 2007).

Barred galaxies offer a useful tool for investigating the physical conditions that support star-formation in galaxies. The motions in bars are characterised by non-circular motions that push the gas into intersecting orbits, where shocks and star-formation can be triggered. The position and strength of the shocks are determined by the bar potential, the global dynamics within the bar region being driven by the bar. We now have a relatively good understanding of the gas behaviour under a bar potential (e.g.; Pérez et al. 2004) and this knowledge can be used to understand the conditions triggering star-formation. Bars and their surroundings host extreme physical conditions and a variety of ISM environments. They are perfect places to study the link between the conditions favouring star-formation and the galaxy dynamics. Therefore, a panchromatic view revealing the history of star-formation in bars can provide a unique insight into the

Table 1. Log of ground-based Hα observations.

Band	Date	Filter	Exp. time	Seeing
Hα	29 Oct 2007	WFCH6568	3×1200 s	1.4″
R	30 Oct. 2007	HARRIS R	3×250 s	2.1″

links between star-formation and the galaxy dynamics, which may also help us to understand how bars form and evolve.

We present a detailed multiwavelength study of the star-formation in the bar region of NGC 2903 performed by analysing the correlations between the location and ages of the *young* stellar clusters, and the morphology of the bar. This was achieved in turn by analysing the emission in Hα, UV, and 24 μm as well as the optical data from the Sloan Digital Sky Survey (SDSS), in addition to 8 μm and CO ($J = 1-0$) emission.

We have chosen NGC 2903 for this research for a number of reasons: it is close-by (8.9 Mpc; Drozdovsky & Karachentsev 2000) allowing us to achieve high spatial resolution (~43 pc arcsec^{-1}), and is isolated from large companions, preventing major merger effects in the results. Irwin et al. (2009) studied the H I content of NGC 2903 demonstrating that it possesses a large H I envelope of around three times its optical size. They also found a small H I companion 64 kpc away from the galaxy in projection, which adds to a previously known small stellar companion. No clear sign of an interaction has been found so far.

NGC 2903 is an SBd galaxy showing a symmetric strong bar considered typical of this class of galaxies (Laurikainen & Salo 2002). Previous observations have shown large amounts of Hα emission along the bar and not only at the ends of the bar and nuclear region (Sheth et al. 2002). The CO ($J = 1-0$), *Spitzer*, and *GALEX* data available makes this galaxy an ideal target for multiwavelength studies to retrieve insight into the star-formation history of bars.

A previous study by Leon et al. (2008) of the NGC 2903 bar showed that HCN(1−0) is distributed along the bar and at its centre. They compared the star-formation rate ratio of the bar to the centre with the predictions of numerical simulations by Martin & Friedli (1997). This made them propose that the bar in NGC 2903 has an age between 200 and 600 Myr.

The outline of the paper is as follows. In Sect. 2, we present the observational data and in Sect. 3 we analyse the general morphology of NGC 2903. We present our methodology to obtain the bar H II regions and UV emission knots catalogues in Sect. 4. The following section contains the main results regarding the $EW_{Hα}$, star-formation rates, UV colours, and ages of the stellar clusters. In Sect. 6, we discuss our main results and finally present a summary and conclusions.

2. Observations and data reduction

2.1. Hα imaging

The Hα data of NGC 2903 was obtained with the Wide Field Camera at the 2.5 m Isaac Newton Telescope at the Roque de los Muchachos Observatory in October 2007. A summary of the observations is presented in Table 1. The galaxy was observed through a 95 Å width narrowband filter with a total exposure time of 3600 s, and an *R*-band filter, used for the continuum subtraction, with an exposure time of 750 s. We carried out the overscan subtraction, bias, and flatfield correction using
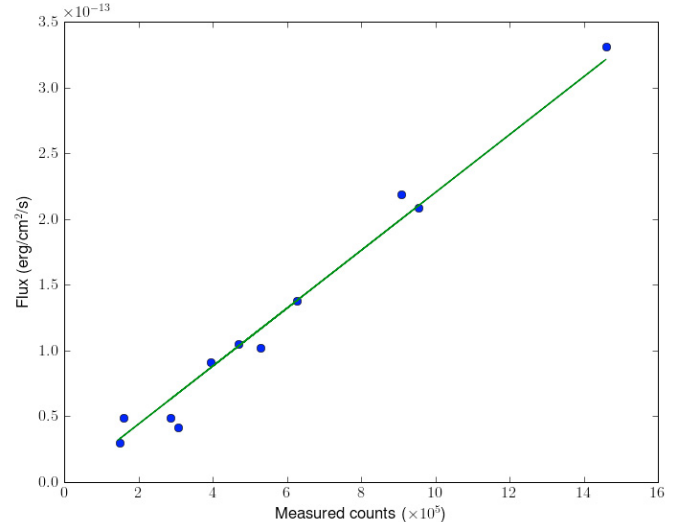
Fig. 1. Scaling relation from our measured Hα+[N II] fluxes in counts to earlier measurements made by Mayya (1994) for the same H II regions. The H II region fluxes measured by Mayya (1994) also include those of the [N II] emission.

standard reduction tasks within IRAF[1]. The sky subtraction was carried out by fitting a first order polynomial to a sky map created using the mean sky values derived from several positions on the image, free of both foreground stars and galaxy emission. The Hα+continuum and *R*-band images were then aligned using the positions of field stars in the images and combined separately to produce the final images. Before continuum subtraction, the Hα+continuum image was degraded to the resolution of the *R*-band image (~2.1″).

The continuum subtraction was done as described by Relaño et al. (2005). We used 11 non-saturated foreground stars in both the Hα (ON-band) and in the continuum *R*-band (OFF-band) images. The fluxes of these stars yielded a mean flux ratio ON-band/OFF-band of 0.34 ± 0.02. This value was then used as a starting point scaling factor to generate a set of OFF-band images scaled with factors ranging from 0.32 to 0.36. These images were afterwards subtracted from the ON-band image to produce images free of continuum emission. After a close inspection of the resulting images, we adopted a value of 0.34 ± 0.01 for the continuum scaling factor. The uncertainty in the continuum scaling factor produces differences of up to ~3% in the integrated fluxes of the H II regions.

The astrometry of the Hα image was performed using the USNO2 catalogue coordinates for the foreground stars of the galaxy images, resulting in an accuracy of ~0.39″. The observations were made during non-photometric conditions. Therefore, for the flux calibration, we used previously reported fluxes of 11 H II regions located in the disk of NGC 2903 published by Mayya (1994). We compared the flux reported there with our measured flux (in ADU) using identical apertures. We then calculated the ratio for each region and assumed the median to be our final Hα flux calibration factor (($2.2 ± 0.4) \times 10^{-19}$ erg s^{-1} cm^{-2} count^{-1}). The error was calculated by taking the standard deviation of the flux ratio for all the stars. The scaling relation is presented in Fig. 1. The 2σ sensitivity limit of the final Hα image is 6.2×10^{-17} erg s^{-1} cm^{-2} per pixel.

---

[1] IRAF is distributed by the National Optical Astronomy Observatories, which is operated by the Association of Universities for Research in Astronomy, Inc. (AURA) under cooperative agreement with the National Science Foundation.

The Hα data of Mayya ([1994](#)) from which our fluxes were flux calibrated were not corrected for Galactic extinction. Therefore, the H II region luminosities of our catalogued H II regions were corrected a posteriori for foreground Galactic extinction (Schlegel et al. [1998](#)), which was assumed to be $A_{Hα} = 0.08$ mag.

The bandwidth of the Hα filter can also be affected by emission from the [N II]$λ6548$ Å and [N II]$λ6584$ Å emission lines at their corresponding redshifted wavelengths. A proper correction for this requires spectroscopic information about all the H II regions, which information is not currently available. The typical [N II]/Hα ratio for extragalactic H II regions of solar metallicity is approximately 0.33 (e.g.; Kennicutt & Kent [1983](#)). Therefore, an approximate correction of 25% should be applied to the Hα fluxes and equivalent widths. Rather than applying this average correction to the fluxes of all H II regions, we decided to present the uncorrected Hα+[N II] luminosities in Table [2](#).

2.2. Spitzer infrared images

To investigate the extinction and the star-formation in the bar of NGC 2903 we used the *Spitzer* 24 μm observations from the Multiband Imaging Photometer (MIPS) instrument (Werner et al. [2004](#); Fazio et al. [2004](#); Rieke et al. [2004](#)). The data was obtained in April 2004 as part of the Local Volume Legacy Survey (Lee et al. [2008](#); Kennicutt et al. [2007](#)). MIPS reduction steps are described in detail by Gordon et al. ([2005](#)). The field of view covered by the observations is large enough to contain the whole galaxy with enough sky coverage allowing a good sky subtraction. The 24 μm point-spread function (PSF) has a measured *FWHM* of ~5.6″ and a $2σ$ sensitivity limit of $0.52 × 10^{-6}$ Jy arcsec^{-2}. The image was registered to the same coordinate system and pixel scale as the Hα image and the background was subtracted in the same way as for the Hα image.

The 24 μm image has a much larger PSF *FWHM* than the Hα image (*FWHM* ~2.1″). Therefore, to allow for accurate comparisons, we produced a convolved version of the Hα image corresponding to the 24 μm PSF by applying a PSF kernel as described by Gordon et al. ([2008](#)). This version image was only used to calculate the Hα attenuation of the H II regions (Sect. [4.3](#)). As complementary data, we also used the 3.6 and 8 μm images, which have a PSF *FWHM* ~ 2″ in both bands. These images were only used to carry out global morphological comparisons with the remaining bands; we therefore registered the images to the same coordinate system as the Hα image, but we did not degrade their spatial resolution.

2.3. GALEX images

To analyse the UV emission and its distribution in NGC 2903, we used *GALEX* mission data (Martin et al. [2005](#)). The *GALEX* direct imaging observations were centered on 1529 Å and 2312 Å for the far-ultraviolet (FUV, 1350−1750 Å) and near-ultraviolet (NUV, 1750−2750 Å) bands, respectively. NGC 2903 was observed in February 2004 as part of the *Nearby Galaxies Survey* (NGS, Bianchi et al. [2003](#)) with an exposure time of 1862 s and 1861 s for the FUV and NUV, respectively. The PSF *FWHM* of the images are ~4.2 and ~4.6″ for the FUV and NUV, respectively, and their respective sensitivity limits $5.25 × 10^{-18}$ and $3.09 × 10^{-18}$ erg s^{-1} cm^{-2} Å^{-1} per pixel (see Bianchi et al. [2003](#) for further details on the NGC 2903 *GALEX* data).

Both the FUV and NUV images were aligned to the same coordinate system and pixel scale as the Hα image and the background was subtracted in the same way as for the Hα and *Spitzer* data.

2.4. Other data: ground-based optical images and CO (J = 1−0)

Ground-based optical images from the *Sloan Digital Sky Survey* (SDSS) and a map of the CO ($J = 1−0$) rotational transition emission were also used for the morphological analysis of NGC 2903. The optical data set comprises g', r', and z' band images, which were observed as part of the SDSS data release 6 and have a PSF *FWHM* of ~1.1″. We subtracted the sky emission from these images using the same IRAF script used for the Hα image (Sect. [2.1](#)).

For the photometric calibration, we estimated the calibration factor for converting the image digital counts to calibrated g', r', and z' AB magnitudes as described on the SDSS web page for the data release 6[2]. These calibrated images were used to produce a $g' − z'$ colour map of NGC 2903 (Fig. [2](#)e).

The CO ($J = 1−0$) emission-line map of NGC 2903 was used to trace the molecular gas emission. It was obtained from the BIMA (Berkeley-Illinois-Maryl and Association) array and the NRAO (National Radio Astronomy Observatory)[3] 12 m single-dish telescope, as part of the BIMA SONG key project. The emission-line map has a maximum *FWHM* of 6.8″. Data acquisition and reduction details can be found in Regan et al. ([2001](#)) and Helfer et al. ([2003](#)).

3. The general morphology of NGC 2903

The different appearance of galaxies in different wavelength ranges has already been illustrated by many authors. Galaxies in the UV bands seem to be patchier and of later type than the same galaxies observed at optical and near-infrared wavelengths. Stellar components such as bulges, bars, and old stellar disks tend to disappear when observed in the UV range (e.g.; Kuchinski et al. [2000](#)). NGC 2903 provides a good example of this behaviour. Figure [2](#) shows NGC 2903 observed in different wavelength regimes: FUV, NUV, 3.6 μm, 24 μm, $g' − z'$ colour map and a CO ($J = 1−0$) rotational transition emission-line map. All images contain superimposed Hα contours.

The UV distribution is patchy and spiral-like and does not resemble the smooth bar-like distribution shown in the 3.6 μm image. The CO ($J = 1−0$) traces the 3.6 μm emission, while the Hα follows an s-shape distribution that is also followed by the main dust-lanes, as shown by the $g' − z'$ colour image. Dust spurs emerge from the main dust lanes at many locations.

The Hα emission leads the CO ($J = 1−0$) emission, taking into account that NGC 2903 rotates counter-clockwise (Hernandez et al. [2005](#)), assuming trailing spiral arms.

4. Photometry of star-forming regions

4.1. HII region catalogue

To study the properties of the recent star-forming sites in the NGC 2903 bar, we produced a catalogue of the H II regions located in the bar zone (except the nucleus). We consider the bar zone to be the area covering the whole *lens region* (Kormendy [1979](#)) as observed in the 3.6 μm image (see Fig. [2](#)c).

---

[2] http://www.sdss.org/dr6/algorithms/fluxcal.html

[3] The National Radio Astronomy Observatory is a facility of the NSF operated under cooperative agreement by Associated Universities, Inc.

Table 2. H II region catalogue of the bar zone of NGC 2903.

ID	RA (J2000)	Dec (J2000)	Radius (arcsec)	e	PA (deg)	$\log L_{H_\alpha+[NII]}$ (in erg s^{-1})	$\log EW_{H_\alpha+[NII]}$ (in Å)	$\log(L_{24\,\mu m})$ (erg s^{-1})	$A_{H\alpha}$ (mag)	SFR ($10^{-3}\,M_\odot$ yr^{-1})
1	09:32:12.35	21:31:04.66	3.1	0	90	38.99 ± 0.05	2.32 ± 0.11	40.60	1.21	17.7 ± 0.9
2	09:32:11.69	21:30:40.84	5.23	0.51	158	39.41 ± 0.05	2.86 ± 0.02	40.93	1.07	41.0 ± 2.2
3	09:32:11.67	21:30:12.75	3.17	0	0	38.71 ± 0.10	–	40.24	1.09	8.3 ± 0.9
4	09:32:12.56	21:30:29.23	3	0	0	38.75 ± 0.08	2.70 ± 0.09	40.19	0.95	7.9 ± 0.8
5	09:32:08.77	21:29:39.86	7.3	0.81	–28	39.28 ± 0.08	2.34 ± 0.04	40.71	0.93	26.5 ± 2.9
6	09:32:07.62	21:29:33.54	3.1	0	0	38.81 ± 0.08	3.07 ± 0.03	40.35	1.09	10.5 ± 0.9
7	09:32:14.38	21:30:40.38	4.23	0.68	6	38.76 ± 0.12	–	40.24	1.01	8.6 ± 1.2
8	09:32:13.75	21:31:02.56	5.23	0.8	–48	38.87 ± 0.11	–	39.49	0.21	5.3 ± 1.5
9	09:32:13.83	21:31:09.62	2.33	0	0	38.43 ± 0.10	2.50 ± 0.01	39.32	0.36	2.2 ± 0.5
10	09:32:12.57	21:30:52.67	4.17	0.77	10	38.60 ± 0.14	–	40.05	0.96	5.7 ± 1.0
11	09:32:13.60	21:30:24.86	3.7	0.52	38	38.62 ± 0.14	–	40.01	0.88	5.6 ± 1.1
12	09:32:07.12	21:29:26.37	2.03	0	0	38.12 ± 0.16	2.28 ± 0.01	39.65	1.08	2.1 ± 0.4
13	09:32:11.43	21:30:00.36	3.1	0	0	38.55 ± 0.14	–	39.97	0.92	4.9 ± 0.9
14	09:32:12.44	21:30:40.75	3	0	0	38.70 ± 0.09	2.43 ± 0.14	40.13	0.93	7.0 ± 0.8
15	09:32:12.63	21:30:36.70	2.23	0	0	38.30 ± 0.13	–	39.70	0.90	2.7 ± 0.5
16	09:32:05.59	21:28:54.01	2.8	0	90	38.59 ± 0.10	2.87 ± 0.03	39.77	0.61	4.1 ± 0.7
17	09:32:07.77	21:28:56.02	3.93	0	0	38.87 ± 0.11	–	40.51	1.27	14.1 ± 1.4
18	09:32:07.56	21:29:11.66	2.6	0	0	38.33 ± 0.16	–	40.23	1.74	6.4 ± 0.6
19	09:32:07.83	21:29:26.69	3.57	0	90	38.66 ± 0.14	–	40.32	1.30	9.0 ± 1.2
20	09:32:12.01	21:30:17.87	2.87	0.85	3	38.22 ± 0.13	–	39.79	1.14	2.8 ± 0.4
21	09:32:12.35	21:30:22.63	2.7	0.78	108	38.25 ± 0.13	2.60 ± 0.09	39.49	0.68	2.0 ± 0.4
22	09:32:13.76	21:30:18.72	1.9	0	0	38.00 ± 0.18	–	39.22	0.66	1.1 ± 0.3
23	09:32:11.44	21:31:11.46	2.33	0	90	38.30 ± 0.14	–	39.87	1.15	3.4 ± 0.5
24	09:32:08.76	21:28:46.76	3.53	0	90	39.10 ± 0.05	2.31 ± 0.04	40.50	0.89	16.8 ± 1.2
25	09:32:07.88	21:28:47.69	3.93	0	0	39.02 ± 0.07	2.63 ± 0.01	40.59	1.15	18.0 ± 1.4
26	09:32:11.67	21:31:27.14	3.6	0	0	38.77 ± 0.11	–	40.39	1.23	10.8 ± 1.2
27	09:32:09.59	21:28:47.12	4.17	0	0	39.41 ± 0.03	2.44 ± 0.02	40.93	1.08	40.8 ± 1.6
28	09:32:10.62	21:31:31.74	3.5	0	90	38.62 ± 0.15	2.56 ± 0.04	40.20	1.17	7.2 ± 1.1
29	09:32:10.18	21:28:42.26	3.1	0	90	38.52 ± 0.15	2.31 ± 0.03	40.13	1.21	6.0 ± 0.9
30	09:32:08.53	21:31:30.16	2.53	0	0	38.46 ± 0.11	2.44 ± 0.06	40.10	1.27	5.5 ± 0.6
31	09:32:11.20	21:28:57.28	3.67	0	0	39.19 ± 0.04	2.67 ± 0.03	40.59	0.89	20.7 ± 1.2
32	09:32:11.67	21:28:30.75	3.7	0	0	38.84 ± 0.10	2.67 ± 0.07	39.62	0.29	5.3 ± 1.3
33	09:32:12.57	21:28:38.22	3.5	0	0	39.14 ± 0.04	2.76 ± 0.02	40.56	0.91	19.1 ± 1.1
34	09:32:13.09	21:28:43.61	3.83	0	0	39.24 ± 0.04	2.49 ± 0.03	40.19	0.41	14.8 ± 1.4
35	09:32:07.93	21:28:16.18	2.67	0	0	38.34 ± 0.17	2.63 ± 0.00	39.73	0.88	2.9 ± 0.7
36	09:32:09.63	21:31:06.38	6.4	0	90	39.81 ± 0.03	2.51 ± 0.02	41.47	1.29	126.1 ± 3.8
37	09:32:08.43	21:31:42.49	2.8	0	90	38.61 ± 0.10	–	39.67	0.50	3.8 ± 0.7
38	09:32:08.81	21:30:55.01	4	0	0	39.14 ± 0.06	2.52 ± 0.08	40.51	0.85	17.8 ± 1.5
39	09:32:09.08	21:31:14.75	2.17	0	0	38.35 ± 0.11	–	40.07	1.41	4.9 ± 0.4
40	09:32:12.38	21:31:30.57	2.33	0	0	38.30 ± 0.14	–	38.98	0.24	1.5 ± 0.5
41	09:32:11.97	21:31:21.00	2	0	0	38.22 ± 0.12	–	39.68	0.98	2.4 ± 0.4
42	09:32:08.06	21:28:42.43	3.67	0	0	38.87 ± 0.09	2.25 ± 0.01	40.32	0.97	10.7 ± 1.2
43	09:32:13.40	21:28:46.21	3.83	0	0	39.16 ± 0.05	2.41 ± 0.03	40.20	0.48	13.4 ± 1.4
44	09:32:09.01	21:28:40.08	2.37	0	0	38.52 ± 0.09	–	40.38	1.67	9.2 ± 0.5
45	09:32:11.96	21:29:10.88	3.27	0	0	38.90 ± 0.07	2.64 ± 0.02	40.55	1.27	15.3 ± 1.0
46	09:32:10.39	21:31:11.67	3.7	0	0	38.79 ± 0.11	2.43 ± 0.04	40.42	1.25	11.5 ± 1.3
47	09:32:13.05	21:31:35.10	2.43	0	0	38.28 ± 0.16	2.85 ± 0.01	39.45	0.62	2.0 ± 0.5
48	09:32:13.47	21:31:32.35	2.7	0	0	38.53 ± 0.11	–	40.00	0.99	5.0 ± 0.7
49	09:32:13.32	21:31:21.74	2.4	0	0	38.19 ± 0.19	2.72 ± 0.09	39.47	0.73	1.8 ± 0.5
50	09:32:09.09	21:28:31.92	3.03	0	0	38.42 ± 0.18	–	40.34	1.80	8.1 ± 0.9
51	09:32:12.27	21:30:08.09	2.7	0.03	83	38.21 ± 0.23	–	39.72	1.04	2.5 ± 0.7
52	09:32:08.58	21:31:34.64	2.67	0	0	38.56 ± 0.10	–	40.10	1.09	5.9 ± 0.7
53	09:32:11.28	21:31:16.48	2.5	0	0	38.17 ± 0.21	2.21 ± 0.36	39.93	1.48	3.4 ± 0.6
54	09:32:12.06	21:31:11.01	3.67	0	0	38.53 ± 0.20	1.99 ± 0.11	40.29	1.47	7.8 ± 1.2
55	09:32:10.77	21:29:56.08	2.5	0	0	38.27 ± 0.17	1.85 ± 0.21	40.29	2.00	6.9 ± 0.6
56	09:32:11.01	21:30:03.02	3.2	0	0	38.51 ± 0.16	–	40.63	2.21	14.6 ± 0.9
57	09:32:12.42	21:29:30.64	3.17	0	0	38.47 ± 0.17	–	40.11	1.26	5.6 ± 0.9
58	09:32:12.10	21:29:33.70	2.67	0	0	38.18 ± 0.24	3.15 ± 0.07	39.70	1.06	2.4 ± 0.7
59	09:32:12.12	21:29:26.71	2.6	0	0	38.12 ± 0.26	–	39.78	1.30	2.6 ± 0.6

The selection criteria for identifying a feature in the Hα image as an H II region is that the feature must have an area in pixels equal to or larger than the image spatial resolution (i.e.; area ≈32 pixels; with a pixel size of 0.33″/pix), all pixels having an intensity of at least three times the r.m.s. noise above the local background intensity level. This selection criteria implies a detectability limit of ~8.3×10^{37} erg s^{-1}.

Table 2. continued.

ID	RA (J2000)	Dec (J2000)	Radius (arcsec)	e	PA (deg)	$\log L_{H_\alpha+[NII]}$ (in erg s^{-1})	$\log EW_{H_\alpha+[NII]}$ (in Å)	$\log(L_{24\,\mu m})$ (erg s^{-1})	A_{H_α} (mag)	SFR ($10^{-3}\ M_\odot$ yr^{-1})
60	09:32:12.21	21:29:17.71	2.43	0	0	38.06 ± 0.26	–	39.92	1.67	3.2 ± 0.5
61	09:32:11.56	21:29:16.67	3.2	0	0	38.32 ± 0.25	2.85 ± 0.06	40.03	1.38	4.4 ± 0.9
62	09:32:10.49	21:28:57.76	3.07	0.55	61	38.27 ± 0.21	2.29 ± 0.05	39.43	0.60	1.9 ± 0.7
63	09:32:07.53	21:29:19.29	4.9	0.9	–18	38.33 ± 0.25	2.46 ± 0.04	40.10	1.50	5.0 ± 1.0
64	09:32:07.53	21:29:04.49	4.63	0.87	14	38.37 ± 0.23	–	40.16	1.54	5.8 ± 1.0
65	09:32:08.01	21:30:28.55	4.13	0	90	38.83 ± 0.13	–	39.96	0.56	6.7 ± 1.6
66	09:32:08.18	21:30:42.83	2.67	0	0	38.16 ± 0.25	–	39.09	0.39	1.2 ± 0.7
67	09:32:12.63	21:29:25.61	2.33	0	0	38.13 ± 0.21	–	39.50	0.86	1.7 ± 0.5

Notes. Column 1: ID number of the catalogued H II regions; Cols. 2 and 3: equatorial coordinates; Col. 4: H II region radius in arcseconds; Cols. 5 and 6: eccentricity and position angle (measured North-West) of the integration apertures; Col. 7: decimal logarithm of the Hα luminosity (in erg s^{-1}); Col. 8: decimal logarithm of the Hα equivalent width; Col. 9: decimal logarithm of the 24 μm emission within the H II region apertures; Col. 10: Hα attenuation see Sect. 4.3; Col. 11: estimate of the current star-formation rate for each catalogued H II region. Columns 7−10 include the corresponding correction for Galactic extinction (Schlegel et al. 1998). The SFRs were obtained after applying a correction of 25% for [N II] contamination to the Hα luminosities and dust extinction as given in Col. 10.

A total of 67 H II regions were catalogued and their positions, sizes, and luminosities were measured. We performed aperture photometry using GAIA[4]. Most of the catalogued regions are located in the s-shape region and its neighbourhood, a region which is closely related to the stellar bar. A representation of the catalogued H II regions can be seen in Fig. 3.

The H II region catalogue comprises the position, size, shape, and Hα+[N II] luminosity of the regions, and is presented in Table 2. The table contains the H II region identification number in Col. 1; the equatorial coordinates (Cols. 2 and 3). Column 4 shows the radius in arcseconds; Cols. 5 and 6 the eccentricity and position angle (measured northwest) of the integration aperture, and Col. 7 shows the decimal logarithm of the Galactic extinction-corrected Hα+[N II] luminosity (not corrected for internal dust extinction).

4.1.1. Hα equivalent width

The Hα equivalent width (hereinafter $EW_{H\alpha}$) is a measure of the strength of the Hα emission with respect to the continuum emission of the stellar ionizing cluster. The $EW_{H\alpha}$ depends not only mainly on the evolutionary stage of the H II region (decreasing as the region ages), but also on the metallicity, the IMF, dust content, and ionizing photon leakage (e.g.; Bresolin & Kennicutt 1999; Zurita & Pérez 2008).

The Hα EWs were calculated from the ratio of our measured Hα luminosities (not corrected for internal dust extinction) to the continuum emission per Å. The continuum emission of the ionizing cluster was estimated from the broad-band emission in the R-band at the position of the catalogued H II regions. Rather than using our Johnson R-band image of NGC 2903, we used the Sloan Digital Sky Survey (SDSS) r'-band image. The latter has a higher spatial resolution than our image, and therefore allowed us to more clearly identify and measure the continuum cluster emission.

When computing the Hα EW of an H II region, we are interested only in the continuum radiation emitted by the ionizing cluster. However, both the flux from the ionizing cluster and the continuum emission from the underlying stellar population of the galaxy are included within the integration apertures. Correcting for this contamination is not straightforward and is

the major source of uncertainty in H II region broad-band fluxes (Zurita & Pérez 2008). We followed the procedure described in Zurita & Pérez (2008) to estimate the contribution of the underlying stellar population to our measured broad-band fluxes by using two of the methods described there.

The first method consists of the measurement of the local background from the median value within annular apertures around the H II regions. The inner radius was set to be the effective radius of the H II region, and the annulus width to approximately three times the H II region radius.

The areas of the image corresponding to catalogued H II regions had previously been masked out in the image to avoid contamination within the annular apertures from neighbouring H II regions. For some regions, the median continuum emission within the annulus is clearly overestimated causing an underestimation of the cluster continuum emission, which sometimes even results in negative fluxes. This is generally due to the strong spatial variations in the disk continuum emission on small scales. Therefore, a second approach was adopted to more tightly constrain the local background estimates.

The second method uses growth curves and takes advantage of the continuum emission in most H II regions being less extended than the Hα emitting area. Therefore, the local background can be obtained from within the H II region area defined by its Hα emission. For each H II region, we derived radially averaged r'-band surface-brightness profiles. For each region, we selected a radial range that was not contaminated by the ionizing cluster and determined the local background surface brightness from a fit to the profile in that range.

The r'-band continuum fluxes were all corrected for the underlying stellar population contamination using both methods (when possible), giving us two estimates of the r'-band flux of the ionizing cluster, from which we derived two values for the $EW_{H\alpha+[NII]}$. We calculated the difference between the two $EW_{H\alpha+[NII]}$ estimates of each H II region, and this was taken to be the measured Hα+[N II] EW uncertainty, so it represents the range of values covered when using the different estimates. Those regions for which the two estimates yielded differences larger than 600 Å, and those regions for which only one background measurement was available, were discarded, as we considered the results non-reliable. The resulting Hα EWs (including emission from the N II lines) are presented in Col. 8 of Table 2.

---

[4] GAIA is a derivative of the Skycat catalogue and image display tool, developed as part of the VLT project at ESO. Skycat and GAIA are free software under the terms of the GNU copyright.
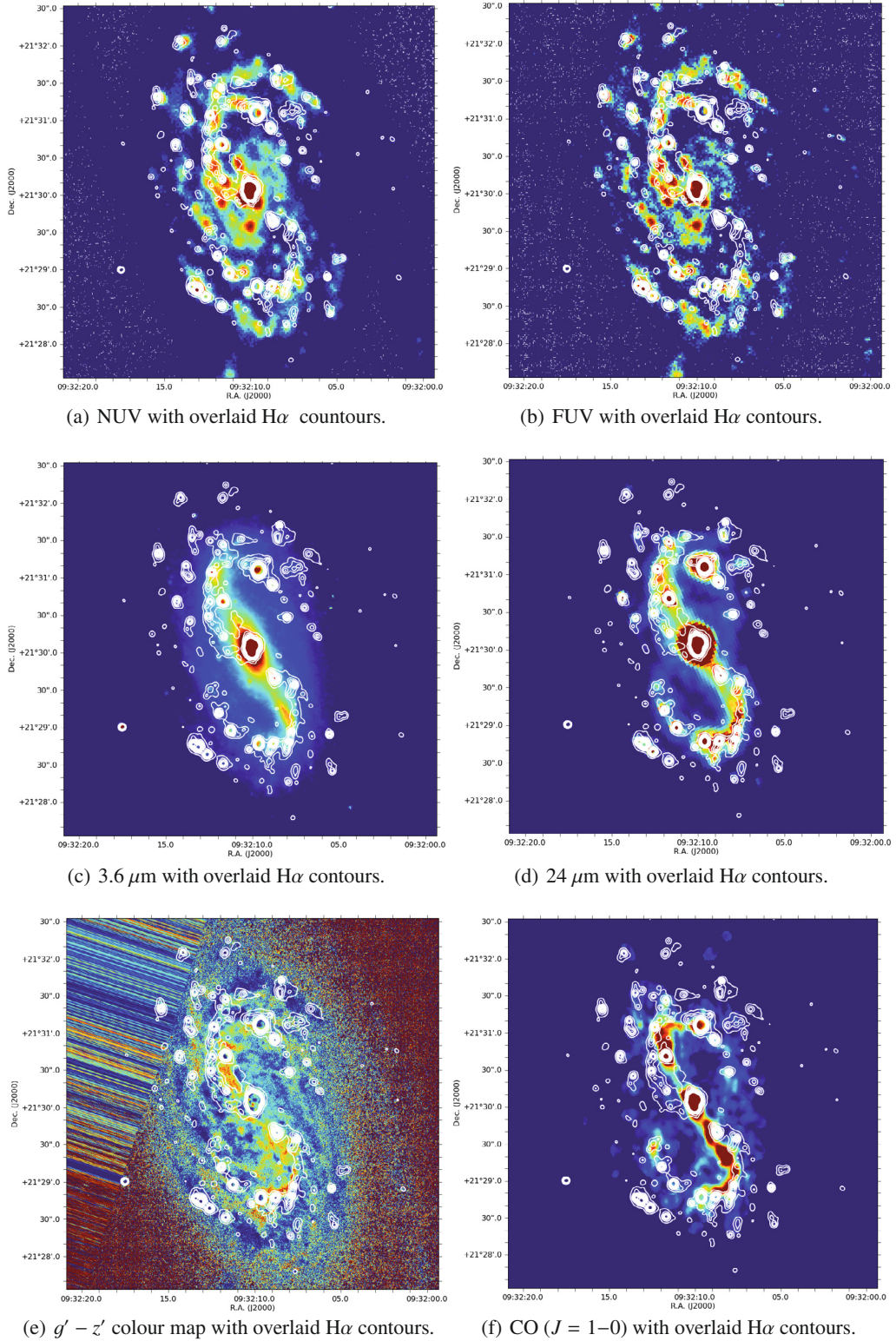
(a) NUV with overlaid Hα countours.

(b) FUV with overlaid Hα contours.

(c) 3.6 μm with overlaid Hα contours.

(d) 24 μm with overlaid Hα contours.

(e) $g' - z'$ colour map with overlaid Hα contours.

(f) CO ($J = 1-0$) with overlaid Hα contours.

Fig. 2. Images of NGC 2903 in different spectral bands: **a)** *GALEX* NUV image, logarithmic scale **b)** *GALEX* FUV image, logarithmic scale **c)** *Spitzer* 3.6 μm **d)** *Spitzer* 24 μm **e)** $g' - z'$ colour−map **f)** CO ($J = 1-0$) transition map of NGC 2903. All the colour scales are given in arbitrary units. All images **a)** to **f)** show superimposed Hα contours, the resolution of each image is given in the text, Sect. 2. The Hα contour levels range between 4.5×10^{35} erg/s/pix and 4.5×10^{36} erg/s/pix (the Hα image pixel size is 0.33″/pix).

4.2. UV photometry

We performed aperture photometry on the NUV and FUV *GALEX* images to catalogue all the UV emitting knots of the bar region with the aim of obtaining their luminosities and

colours. The aperture photometry was performed as described in Sect. 4.1 for the H II region catalogue, but using circular apertures centered on the FUV peaks. The location of the apertures is shown in Fig. 4. The same apertures and centres were used to measure fluxes on the Hα and 24 μm with the
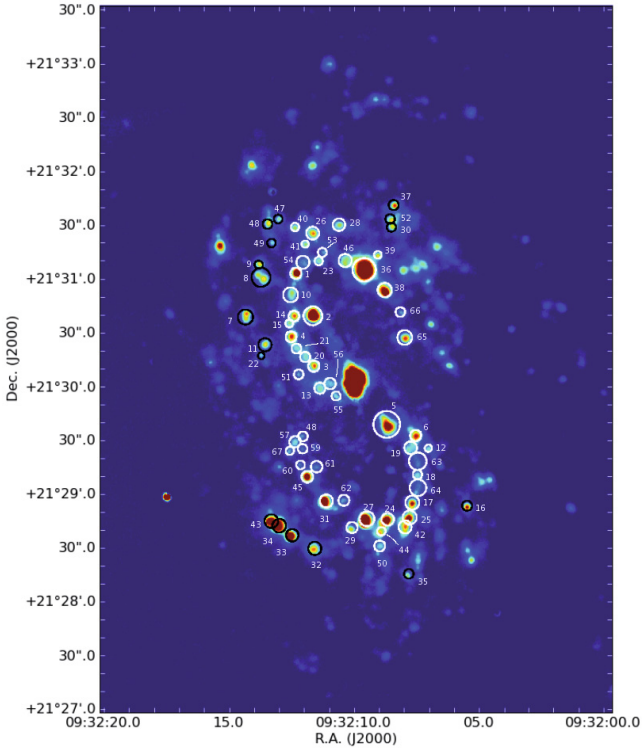
Fig. 3. Hα continuum-subtracted image of NGC 2903. The white open circles indicate the position and size of the integration apertures of the catalogued H II regions belonging to the bar region. The black open circles indicate the H II regions closest to the catalogued UV complexes without Hα counterparts.

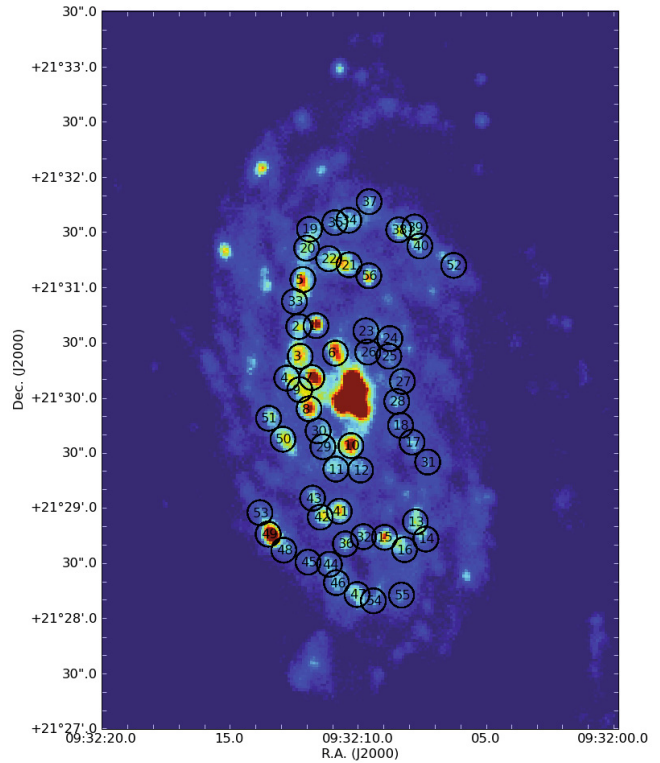**Fig. 4.** *GALEX* NUV image of NGC 2903 with the apertures used for photometry in the FUV, NUV, Hα, and 24 μm images. See Sect. 4.2 for further details.

aim of deriving the dust attenuation (Sect. 4.3). The aperture size selection, 13.2 arcsec, corresponding to ∼570 pc at the galaxy distance, was determined by the spatial resolution of the 24 μm image and the emission peak shifts of the emitting knots at the different bands (see below in this section). These large apertures can cause some overlap between integration areas of neighbouring regions, but in none of the cases is the contamination significant.

As already mentioned for the Hα photometry in Sect. 4.1, the background emission has to be subtracted from the measured 24 μm, NUV, and FUV fluxes within the aperture, to yield the stellar cluster emission alone. When estimating the background contamination, the annuli around each aperture are difficult to define because of crowding. As an alternative method, we fitted light profiles perpendicular to the bar major axis averaged over a rectangle of width ≈40″ (much larger than our photometric apertures for averaging out small-scale background variations, but small enough to ensure a valid local background estimate). The local background of each region was then obtained by interactive interpolation of the background on the corresponding fitted profile (second order polynomial) at the position of the emission peaks. A total of 56 regions were catalogued in the bar region alone (excluding the galaxy centre) and the positions, luminosities, and UV colours are shown in Table 3.

The peaks of emission in the UV and the 24 μm (and Hα) image are offset from each other by a few arcseconds in most of the regions. This offset between the emission peaks in UV and 24 μm (and Hα) amounts to 6″ and was already noticed by Calzetti et al. (2005) for M 51.

As already said, the 24 μm and Hα emission peaks do not always fall within the UV apertures. Therefore, the Hα and 24 μm

luminosities shown in Table 3 should be used with care, as they represent the luminosities of regions centered on the UV peaks with the unique aim of obtaining the dust attenuation in the UV. For the Hα luminosities of the H II regions, we refer the reader to Sect. 4.1 and Table 2. Last column of Table 3 shows the ID number of the H II region catalogue, which matches the UV emitting knot.

A careful visual inspection of the UV, the Hα, and the 24 μm images of NGC 2903 indicates that a number of compact bright UV emission knots, mainly located in the bar region, in the southeastern and northwestern area from the nucleus, have significant counterpart emission at neither Hα nor 24 μm wavelengths (see Fig. 2).

4.3. Dust attenuation

For many years, much effort has gone into deriving reliable and easy-to-use dust extinction indicators to correct optical and UV observations (e.g.; Kennicutt 1983; Calzetti et al. 2000; Iglesias-Páramo et al. 2006). The appearance of multiwavelength observations from the FUV to the mid-infrared of a relatively large sample of nearby galaxies (e.g.; SINGS; Kennicutt et al. 2003) allowed us to determine a reliable extinction correction using all the available bands. The Hα and 24 μm combination has been shown to be a very useful tool for estimating attenuation-corrected Hα and UV fluxes (Kennicutt et al. 2007, 2009). We used these results to obtain dust-corrected UV fluxes. We calculated the attenuation in the UV bands from the Hα attenuation using the laws presented by Calzetti (2001)

$$A_{0.16,\text{star}} = 1.78 A_{\text{H}\alpha,\text{gas}} \quad \text{(FUV)}$$

$$A_{0.28,\text{star}} = 1.29 A_{\text{H}\alpha,\text{gas}} \quad \text{(NUV)},$$

Table 3. Summary of positions and photometry of the star-forming knots.

ID	RA (J2000)	Dec (J2000)	$\log L_{H\alpha}$ (erg s^{-1})	$\log L_{24\,\mu m}$ (erg s^{-1})	$\log L_{FUV}$ (erg s^{-1})	$\log L_{NUV}$ (erg s^{-1})	$A_{H\alpha}$ (mag)	FUV (mag)	NUV (mag)	FUV–NUV (mag)	Hα ID
1	09:32:11.67	21:30:40.80	39.15	40.92	40.63	40.73	1.27	15.74	15.67	0.08	2
2	09:32:12.34	21:30:40.00	38.93	40.57	40.53	40.61	1.06	16.37	16.22	0.15	14, 15
3	09:32:12.25	21:30:23.80	38.87	40.32	40.80	40.83	0.78	16.19	16.03	0.16	4, 20, 21
4	09:32:12.75	21:30:11.70	<38.48	<39.41	40.65	40.58	0	17.95	17.68	0.27	–
5	09:32:12.23	21:31:05.70	38.94	40.71	40.74	40.81	1.29	15.44	15.45	–0.01	1
6	09:32:10.89	21:30:26.10	38.65	40.47	40.69	40.83	1.36	15.44	15.30	0.14	–
7	09:32:11.78	21:30:12.50	38.86	40.32	40.90	40.91	0.8	15.89	15.81	0.08	2, 3
8	09:32:11.85	21:29:55.30	<38.48	<39.53	40.77	40.80	0	17.65	17.13	0.52	13
9	09:32:12.23	21:30:05.70	<38.48	<39.75	40.71	40.74	0	17.79	17.26	0.53	51
10	09:32:10.18	21:29:35.90	<38.48	<39.82	40.79	40.87	0	17.59	16.95	0.64	–
11	09:32:10.74	21:29:22.90	<38.48	<38.94	40.41	40.54	0	18.55	17.78	0.77	–
12	09:32:09.78	21:29:22.80	<38.48	<39.53	40.32	40.41	0	18.77	18.10	0.67	–
13	09:32:07.59	21:28:55.40	38.97	40.64	40.52	40.64	1.11	16.29	16.08	0.21	17
14	09:32:07.16	21:28:46.10	38.75	40.03	40.43	40.46	0.6	17.45	17.21	0.23	25
15	09:32:08.77	21:28:46.40	39.17	40.84	40.64	40.71	1.1	16.00	15.91	0.09	24
16	09:32:07.98	21:28:40.00	38.88	40.51	40.54	40.59	1.06	16.35	16.29	0.06	42
17	09:32:07.81	21:29:38.70	38.90	40.38	40.09	40.23	0.83	17.88	17.49	0.39	–
18	09:32:08.27	21:29:47.70	38.87	40.26	40.05	40.14	0.71	18.18	17.86	0.33	–
19	09:32:12.03	21:31:33.30	38.70	40.34	40.54	40.58	1.07	16.31	16.31	0.01	26
20	09:32:12.12	21:31:22.90	38.70	40.49	40.64	40.68	1.32	15.63	15.72	–0.1	41
21	09:32:10.45	21:31:14.50	38.83	40.70	40.65	40.75	1.45	15.36	15.38	–0.03	46
22	09:32:11.25	21:31:17.50	38.78	40.39	40.62	40.74	1.02	16.20	15.95	0.25	23
23	09:32:09.72	21:30:38.80	<38.48	<39.53	40.19	40.34	0	19.10	18.27	0.82	–
24	09:32:08.78	21:30:34.90	<38.48	<39.84	40.26	40.27	0	18.91	18.44	0.48	–
25	09:32:08.80	21:30:25.20	<38.48	<39.94	40.17	40.20	0	19.15	18.63	0.52	–
26	09:32:09.63	21:30:27.20	<38.48	<40.07	40.12	40.27	0	19.28	18.44	0.84	–
27	09:32:08.25	21:30:11.70	<38.48	<39.85	40.09	40.06	0	19.35	18.96	0.39	–
28	09:32:08.45	21:30:00.70	<38.48	<40.06	40.17	40.20	0	19.16	18.61	0.55	–
29	09:32:11.27	21:29:34.90	<38.48	<39.52	40.37	40.44	0	18.64	18.02	0.62	–
30	09:32:11.47	21:29:43.50	<38.48	<39.81	40.39	40.36	0	18.59	18.22	0.37	–
31	09:32:07.17	21:29:28.20	38.83	40.24	39.79	39.94	0.74	18.77	18.31	0.46	6
32	09:32:09.60	21:28:46.50	39.16	41.03	40.37	40.44	1.45	16.06	16.16	–0.09	27
33	09:32:12.54	21:30:53.60	38.76	40.63	40.45	40.59	1.46	15.84	15.75	0.09	10
34	09:32:10.51	21:31:38.80	<38.48	<40.07	40.58	40.64	0	18.12	17.54	0.59	28
35	09:32:11.05	21:31:37.20	<38.48	<40.19	40.54	40.58	0	18.22	17.67	0.56	–
36	09:32:10.29	21:28:42.20	38.62	40.53	40.40	40.47	1.53	15.84	15.98	–0.14	29
37	09:32:09.74	21:31:49.20	<38.48	<39.48	40.42	40.49	0	18.52	17.89	0.63	–
38	09:32:08.56	21:31:34.30	38.76	40.44	40.61	40.65	1.12	16.05	16.06	–0.01	30, 52
39	09:32:07.94	21:31:36.10	38.82	40.01	40.59	40.61	0.5	17.20	16.97	0.23	37
40	09:32:07.72	21:31:25.80	<38.48	<39.31	40.54	40.60	0	18.22	17.63	0.59	–
41	09:32:10.56	21:28:59.90	38.92	40.38	40.67	40.72	0.81	16.48	16.28	0.19	–
42	09:32:11.30	21:28:56.40	38.90	40.76	40.64	40.66	1.42	15.46	15.64	–0.18	31
43	09:32:11.61	21:29:06.70	38.75	40.52	40.47	40.51	1.27	16.15	16.20	–0.05	45
44	09:32:10.89	21:28:30.90	<38.48	<40.03	40.52	40.52	0	18.28	17.82	0.47	–
45	09:32:11.72	21:28:31.70	38.74	40.16	40.39	40.36	0.76	17.26	17.24	0.01	32
46	09:32:10.59	21:28:21.00	<38.48	<39.53	40.55	40.57	0	18.20	17.71	0.49	–
47	09:32:09.78	21:28:14.80	<38.48	<39.74	40.64	40.60	0	17.97	17.61	0.36	–
48	09:32:12.68	21:28:37.90	39.01	40.57	40.54	40.53	0.94	16.55	16.59	-0.04	33
49	09:32:13.30	21:28:46.40	39.07	40.46	41.10	41.04	0.72	15.54	15.60	–0.06	34, 43
50	09:32:12.83	21:29:38.40	38.48	39.71	40.66	40.59	0	17.92	17.64	0.28	–
51	09:32:13.41	21:29:49.60	<38.48	<39.63	40.40	40.33	0	18.57	18.29	0.28	–
52	09:32:06.38	21:31:15.80	38.65	39.77	40.42	40.44	0.43	17.75	17.47	0.28	–
53	09:32:13.65	21:28:58.00	<38.48	<39.77	40.47	40.49	0	18.39	17.90	0.49	–
54	09:32:09.14	21:28:11.60	<38.48	<39.98	40.48	40.47	0	18.38	17.95	0.43	- -
55	09:32:08.05	21:28:15.20	<38.48	<40.14	40.30	40.40	0	18.82	18.11	0.71	35
56	09:32:09.67	21:31:08.80	39.42	41.32	40.25	40.44	1.5	16.26	16.08	0.18	36

Notes. Column 1: ID of the regions; Cols. 2 and 3: right ascension and declination respectively; Cols. 4−7: decimal logarithm of the Hα, 24 μm FUV and NUV luminosities respectively, these values have not been corrected for extinction; Col. 8: estimated Hα attenuation in magnitudes; Cols. 9 and 10: FUV and NUV attenuation-corrected magnitudes; Col. 11: the FUV–NUV colour of the star forming region. Column 4 shows luminosities corrected for a 25% [N II] contamination. For the regions where Col. 8 has a value of 0.0, Cols. 4 and 5 correspond to an upper limit of the corresponding luminosities.
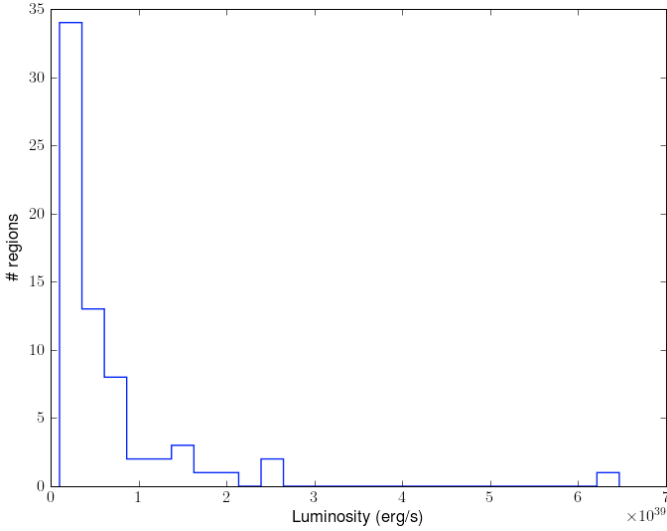
Fig. 5. Distribution of the Hα+[N II] luminosity of the catalogued H II regions across the bar zone of NGC 2903 from which the $EW_{Hα}$ were calculated.

where A_X is the attenuation, in magnitudes, at the specific band. To obtain the Hα attenuation, we used the method described by Kennicutt et al. (2007)

$$A_{Hα} = 2.5 \log\left[1 + \frac{aL_{24\,μm}}{(L_{Hα})_{obs}} \right],$$

where $(L_{Hα})_{obs}$ refers to the observed Hα luminosity with correction for the N II lines, $L_{24\,μm}$ is defined as the product $νL_ν$, and a is the $L_{24\,μm}/L_{Hα}$ constant scaling factor, which is fitted empirically. A value of 0.038 was adopted for a, as derived in the same paper for the derivation of individual region parameters, and a value of $a = 0.02$ was adopted when deriving galaxy integrated parameters. Galactic extinction was applied to the calculation of the dust attenuation. Errors in the attenuation and UV magnitudes follow from two uncertainties; first, the photometric calibration uncertainties and second, the local background estimates. Errors are of the order of 10%.

Because no dust tracers are detected in the UV emitting regions without Hα and 24 μm emission counterparts, we adopted a value of zero for the attenuation in these regions. Besides the lack of Hα and 24 μm, neither 8μm (Dale et al. 2009) nor CO ($J = 1−0$) emission is detected in these regions, indicating that there is very little gas or dust obscuring the UV emission. As an $L_{Hα}$ upper limit for these regions we assumed $L_{Hα+[NII]} = 3.8 \times 10^{38}$ erg s^{-1}, which is the integrated Hα luminosity in a 13.2 arcsec aperture assuming a constant flux per pixel equal to the rms noise of the Hα image background. The derived Hα attenuations for the complete catalogue are presented in Table 3. We then derived UV-corrected magnitudes and calculated the FUV–NUV colour for each region. These results are also presented in Table 3: Col. 1 indicates the ID of the regions; Cols. 2 and 3 the equatorial coordinates; Cols. 4−7 the Hα, 24 μm, FUV, and NUV luminosities, respectively; Col. 8 the Hα attenuation; Cols. 9 and 10 the FUV and NUV attenuation-corrected magnitudes, respectively; Col. 11 the FUV−NUV colour derived; and Col. 12 the H II region ID (taken from Table 2) located close to each of the corresponding UV knot.

5. Results

5.1. Hα luminosity and $EW_{Hα}$

The logarithms of the Hα +[NII] luminosities of the H II regions of NGC 2903 range from 38.0 to 39.8 erg s^{-1} and their distribution is shown in a histogram in Fig. 5. The luminosities are within the range of typical values for extragalactic H II regions in barred and unbarred galaxies (see e.g.; Kennicutt et al. 1989; Mayya 1994; González-Delgado & Pérez 1997; Rozas et al. 1999; Relaño et al. 2005), but are higher than the Hα luminosities reported by Alonso-Herrero et al. (2001) for the nuclear region of NGC 2903. This apparent discrepancy is partly caused by the smaller distance assumed for NGC 2903 by these authors (6.3 Mpc versus 8.9 Mpc assumed in this paper). More importantly, Alonso-Herrero et al. (2001) apply a semi-automated method based on a limiting Hα surface brightness to define the edges of an H II region from an *HST* image, yielding catalogued Hα knots that may correspond to parts of a single H II region, as defined in ground-based Hα imaging, and therefore have lower luminosities and sizes.

The H II region number 36, located in the northernmost part of the bar (see Table 2 and/or Fig. 3), has an Hα luminosity of 6.4×10^{39} erg s^{-1}, which makes this region the brightest H II region in the galaxy (outside the nuclear region of the galaxy). Its luminosity is comparable to, for instance the brightest H II region in the nearby spiral galaxy M 51 (Calzetti et al. 2005; Scoville et al. 2001) and 30 Doradus in the Large Magellanic Cloud (Kennicutt et al. 1989).

The $EW_{Hα+[NII]}$ of H II regions in the bar of NGC 2903 range from ~71 to ~1550 Å, which is typical of disk and bar H II regions (e.g.; Bresolin & Kennicutt 1999; von Hippel & Bothum 1990; Cedrés et al. 2005; Zurita & Pérez 2008). The distribution of $EW_{Hα+[NII]}$ has a mean value of log $EW_{Hα+[NII]}$ = 2.6 ± 0.3 ($EW_{Hα}$ in Å).

The Hα equivalent width of H II regions depends on several factors including the initial mass function (IMF), the evolutionary status of the H II region, its metal content, and ionizing photon loss due to dust extinction or leakage from the region. Zurita & Pérez (2008) analysed the effect of all these factors on the observed distribution of $EW_{Hα}$ for the bar H II regions in NGC 1530, and we refer the reader to that paper for a more detailed discussion of the subject. Assuming similar physical conditions in the bar of NGC 2903, the evolutionary status of the H II region is the dominant factor affecting the $EW_{Hα}$ distribution. Assuming also that the H II region is the product of a single burst of star-formation, population synthesis models such as *Starburst99* (Leitherer et al. 1999) can be used to estimate an average age for each H II region, for a given IMF and metallicity. We therefore compared the theoretical predictions of *Starburst99* for the evolution of a single burst of star-formation with age, with our $EW_{Hα}$ measurements. Our *Starburst99* simulations used the Geneva stellar-evolutionary tracks, and a metallicity of $Z = 0.02$ was assumed, which is the mean oxygen abundance of the gas in NGC 2903 at the range of galactocentric distances covered by the NGC 2903 bar (Pilyugin et al. 2004). For the IMF, we assumed a multi power-law parametrization ($dN/dm \propto m^{-α}$) with $α = 1.35$ for $0.1 < M < 0.5\ M_⊙$ and $α = 2.35$ (Salpeter) for higher masses up to $100\ M_⊙$. From the comparison of the *Starburst99* output with our measurements (after correcting for [N II] contamination), we estimate that the ages of the catalogued H II regions of NGC 2903 are between 2.7 Myr (log $EW_{Hα}$ = 3.07) and 7.1 Myr (log $EW_{Hα}$ = 1.73). We note that to derive an age from the measured equivalent

width, we first had to correct the measured equivalent width of the [N II] lines contribution.

Figure 6 shows the distribution of the EW_{H_α} in the galaxy on top of 3.6 μm intensity contours. As mentioned earlier, the 3.6 μm emission is a strong tracer of old underlying stellar populations and therefore a good indicator of the stellar bar. The distribution of the EW_{H_α} shows no correlation with position within the bar.

5.2. Dust attenuation

Figure 8 presents the distribution and amplitude of the Hα attenuation in the bar of NGC 2903 with the 3.6 μm intensity contours (tracing the stellar bar) overlaid on top. The attenuation was calculated from the ratio of the Hα to the 24 μm emission (Kennicutt et al. 2007) as presented in Sect. 4.3. The apertures are centered on regions of strong UV emission.

The mean attenuation value is around $A_{H_\alpha} \sim 1.0$ mag and ranges from 0 to 1.5 mag (except for regions 55 and 56, closer to the nucleus with an attenuation value of 2.2). There are a few UV regions where we assume no dust attenuation because of a lack of any significant Hα and 24 μm emission (see Sect. 4.3). The higher attenuation values are located in the bar and at the beginning of the spiral pattern (see Table 3). This indicates that the bar and spiral arms in NGC 2903 are gas rich, whereas the UV emitting regions to the northwest and southeast of the galaxy nucleus, those regions with zero attenuation, have low gas and dust content; nevertheless, this region is populated by young stellar clusters, see Sect. 5.4. Additional discussion of the origin of these regions is presented in Sect. 6.

5.3. Star-formation rate

The locations of the most active star-formation sites within a bar are determined by the favoured dynamical behaviour of the gas and dust. Studying the distribution of the loci of current star-formation within bars can therefore put constraints on the properties of a particular bar potential. Gas does not stay in typical bar intersecting orbits and tends to accumulate and shock in certain regions of the bar. Dust lanes can be used as tracers of shocks in the gas flow (Athanassoula 1992). From Fig. 2, one can already see that the dust lanes (as seen from the $g' - z'$ colour map) follow the CO ($J = 1-0$) distribution, the Hα leading the CO ($J = 1-0$) as previously observed in other barred spirals (e.g.; Sheth et al. 2002). The Hα emission in the bar of NGC 2903 follows an s-shape covering the whole stellar bar and is dominated by classical localised H II regions (Fig. 3).

In ionization-bounded H II regions, the reddening-corrected Hα luminosity scales directly with the total Lyman continuum flux emitted by the ionizing embedded star cluster. Therefore, the Hα emission is a good tracer of current star-formation. We used the following calibration relating the Hα luminosity to the rate of star-formation (Kennicutt 1998)

$$SFR_{H_\alpha} (M_\odot \, year^{-1}) = 7.9 \times 10^{-42} \, L_{H_\alpha} (erg \, s^{-1}),$$

for calculating the current SFR associated with each catalogued H II region (Sect. 4.1). The results are given in Col. 11 of Table 2 and were obtained from the observed Hα luminosities (Col. 4 of Table 2), and were corrected for [N II] emission-lines contamination (see Sect. 2.1) and dust extinction inside the regions. The latter were estimated as already described in Sect. 4.3 for the UV emitting knots, comparing the Hα and 24 μm luminosities within the H II region apertures. Given the
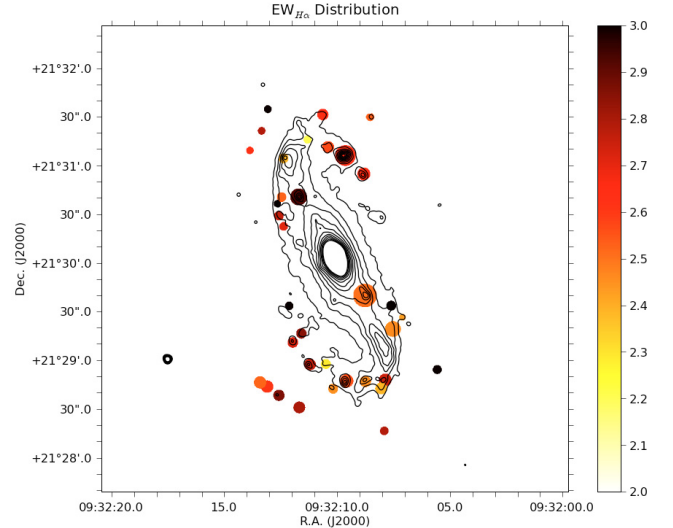
Fig. 6. Hα+[N II] *EW* distribution in the bar region of NGC 2903. The size of the circles represents the H II region projected area. The intensity contours trace the 3.6 μm emission.

different spatial resolution of the two images, we applied an aperture correction factor (Table 1 of Engelbracht et al. 2007). The SFRs obtained for our catalogued H II regions range from $\sim$1.1 to $\sim$126 $\times 10^{-3} \, M_\odot$ year^{-1}. We excluded regions 55 and 56 in this calculation because of likely contamination from the nuclear region emission.

The total SFR implied by the Hα emission of the bar zone of NGC 2903 (excluding the nucleus) is $\sim$0.9 $\pm$ 0.2 $M_\odot$ yr^{-1} (Fig. 7 shows the integration area). This value implies that the NGC 2903 bar is forming stars at a rate comparable to other normal (non-starburst) spirals. The nucleus of NGC 2903 is almost as bright in Hα as the whole bar, implying that it hosts similar SFRs (Alonso-Herrero et al. 2001; Leon et al. 2008).

Alternative SFR calibrations make use of the UV emission. We derived the integrated SFR, within the same region as for the calculation of the SFR_{H_α}, using the UV emission as SF indicator. The SFR in the UV has been computed following the recipes given in Salim et al. (2007)

$$SFR_{UV} (M_\odot \, year^{-1}) = 1.08 \times 10^{-28} \, L_{FUV},$$

with L_{FUV} in erg s^{-1} Hz^{-1}. The star-formation rates calculated in this way infer a $SFR_{FUV} = 0.44 \pm 0.06 \, M_\odot$ yr^{-1} for the bar region. The SFR calculated from both bands (cf. $SFR_{UV} = 0.44 \pm 0.06 \, M_\odot$ yr^{-1} and $SFR_{H_\alpha} = 0.9 \pm 0.2 \, M_\odot$ yr^{-1}) and the fluxes from which these SFR were obtained, are compatible with the results given by other works based on a large number of galaxies (i.e.; Lee et al. 2009; Salim et al. 2007). The SFR_{UV} is a tracer of *recent* star-formation, averaged over some hundreds of Myrs (Calzetti et al. 2005; Kong et al. 2004), while the SFR_{H_α} probes the *current* star-formation. The SFRs derived in this paper are compatible with a number of star-formation histories, as derived from the *Starburst99* model. It is, however, interesting to date the age of the UV complexes with no Hα counterpart to shed some light into the origin of these structures. This is investigated in the next section.

5.4. UV colours and cluster ages

There is now a substantial amount of observational evidence that the FUV−NUV colours are very sensitive to the age of young
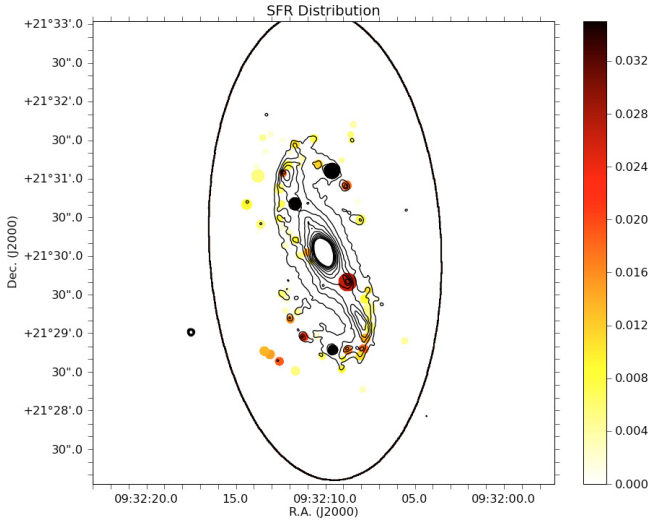
Fig. 7. SFR distribution in the bar region of NGC 2903. The size of the circles represents the H II region projected area. The SFR is given in $M_\odot$ yr^{-1}. The SFR was estimated from the measured Hα luminosity of the H II regions (see Sect. 5.3). The intensity contours trace the 3.6 μm emission. The solid black line indicates the integration area for the calculation of the total SFR in the bar region (see Sect. 5.3)

.

stellar populations because of the rapid evolution of the most massive stars (i.e.; Bianchi et al. 2006; Calzetti et al. 2005). To estimate the ages of our catalogued UV regions, we used the FUV−NUV colours, which had been calculated using fluxes corrected for dust attenuation (Sect. 4.3). Figure 10 shows the range of UV colours in the bar of NGC 2903. The colours have a mean value of 0.3 mag with a standard deviation of 0.27 mag. This range of values is typical of spiral galaxies (Thilker et al. 2005; Koribalski & López-Sánchez 2009). Figure 9 shows the spatial distribution of the derived FUV−NUV regions. One of the most striking properties of the colour distribution are the redder regions located to the northwest and southeast of the galaxy nucleus and at the beginning of the spiral arm. These regions correspond mostly to those with the lowest attenuation. The regions located along the bar consist mostly of blue UV emitting regions.

As well as being age-dependent, the FUV−NUV colours are also strong tracers of metallicity; however, we can assume an approximately constant metallicity in the bar region of NGC 2903 (Pilyugin et al. 2004). With this assumption, the FUV−NUV colour is, as we already mentioned, a good tracer of age. To compare our results with the theoretical models and then derive the ages of the clusters, we model the evolution of a single-star-formation burst using the *Starburst99* population synthesis model (Leitherer et al. 1999). As input values, we used the Padova AGB stellar tracks with a metallicity of $Z = 0.02$ (solar). For the IMF, we assumed a multi power-law parametrization with $\alpha = 1.3$ for $0.1 < M < 0.5\ M_\odot$, and $\alpha = 2.35$ for higher masses up to 100 $M_\odot$. We then derived the FUV−NUV colours from the simulated spectrum in multiple time-steps of between 1 Myr and 1 Gyr (see Fig. 11).

To estimate the UV region ages, we interpolated the modelled FUV−NUV colour versus age dependence to the observed UV colours. The colours of the bluer regions range from −0.18 to 0.15, corresponding to an age of 3 to 10 Myr. The redder regions have colours ranging from 0.4 to 0.85, which imply ages ranging from ~150 to 320 Myr. The latter group of colours corresponds to regions with significant amounts of neither Hα nor 24 μm emission. The FUV−NUV colour
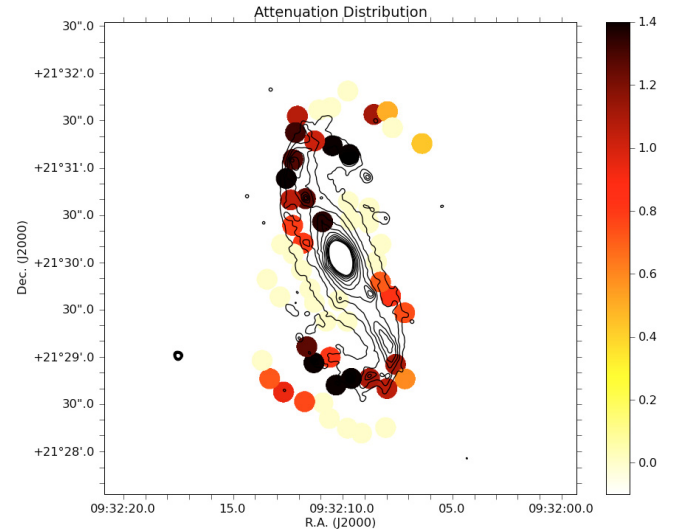

Fig. 8. Distribution of the Hα attenuation in NGC 2903. The circle size represents the integration apertures used for the UV catalogue. The intensity contours trace the 3.6 μm emission.
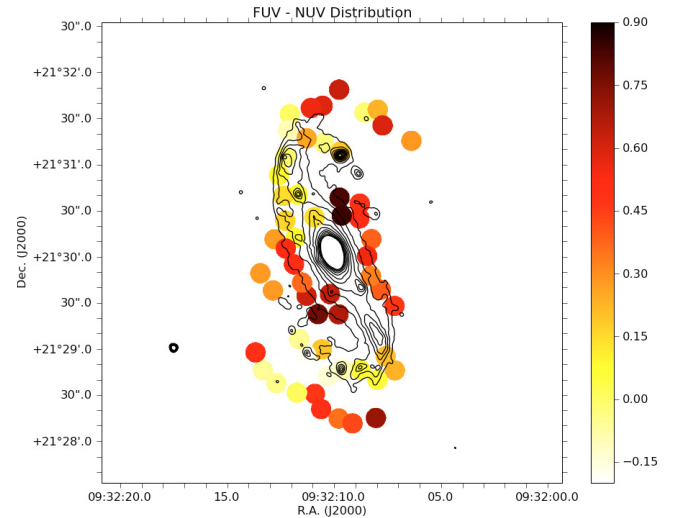

Fig. 9. Distribution of the UV colours in the NGC 2903 bar and its surrounding regions. The intensity contours trace the 3.6 μm emission. A concentration of redder regions is clearly visible to the northeast and southwest of the nucleus. These regions correspond to the UV regions with no significant Hα counterpart.

remains constant around 0.2 implying ages between 10 and a little younger than 100 Myr.

6. Discussion

NGC 2903 is a clear example of a galaxy with very different morphologies as shown by different broad-band images. Although its bar is classified in the NIR with a bar strength of 3 (Laurikainen & Salo 2002), corresponding to a relatively strong bar, and it is considered to be a *classical* bar, its morphology at shorter wavelengths being more similar to that of a patchy spiral disk. This clearly shows that to understand the SF history in bars it is necessary to obtain a panchromatic view.

To investigate the properties of SF in the NGC 2903 bar, we have at our disposal information about the distribution of gas in two different phases, namely the ionised gas and the colder CO ($J = 1-0$). As for the stellar component, we are able to trace
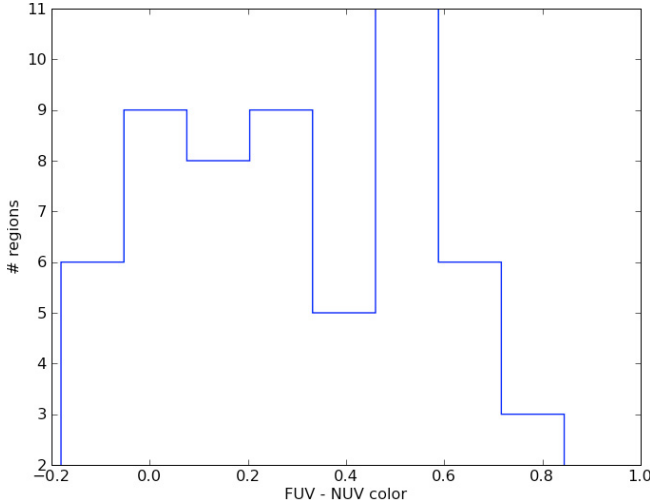
Fig. 10. FUV−NUV colour distribution for the catalogued UV regions in the bar zone of NGC 2903.
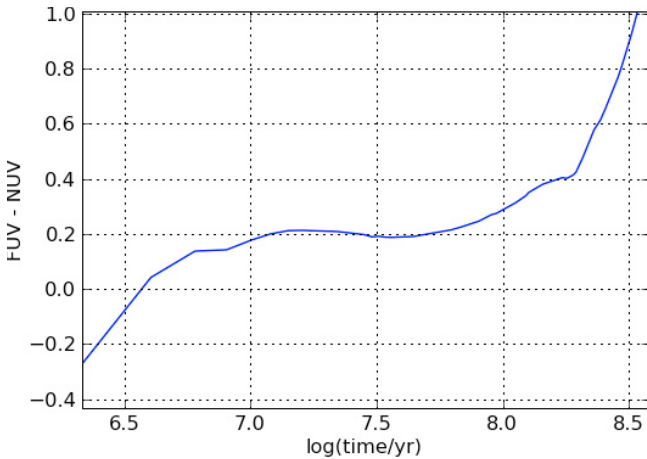

Fig. 11. Time evolution of the UV colour for a single starburst region. The model assumes Padova stellar tracks with $Z = 0.02$ (solar) and an IMF constructed by a multi power-law parametrization with $\alpha = 1.3$ for $0.1 < M < 0.5\ M_\odot$ and $\alpha = 2.35$ for higher masses up to $100\ M_\odot$.

young stars up to 1 Gyr with the UV information, the location of massive stars can be traced from the location of their H II regions, whereas intermediate and older stellar populations can be probed according to their distribution in both the 3.6 μm and optical bands.

We observe that the CO ($J = 1-0$) distribution closely follows the emission in the 3.6 μm band. There is a misalignment between the major axis of the bar derived from ellipse fitting of optical images (Sheth et al. 2002) and the 3.6 μm major-axis light distribution. Both the CO ($J = 1-0$) and the 3.6 μm should therefore be on the leading side of the optical photometric axis of the bar. The Hα emission leads not only both the CO ($J = 1-0$) and the 3.6 μm emission but has a slightly different distribution, following a spiral pattern not so clearly seen in the CO ($J = 1-0$) and 3.6 μm emission. The Hα emission also leads the dust lanes as traced by optical colour maps. Numerical models predict that the gaseous component (of both ionised and neutral gas) leads the stellar bar (Martin & Friedli 1997).

This study started as a follow-up of the analysis carried out on the bar of NGC 1530 (Zurita & Pérez 2008) to understand the physical processes determining star-formation in bars, where the importance of bar dynamics was clearly demonstrated. Both

CO ($J = 1-0$) and dust are concentrated in regions where shocks and gas accumulation are induced by the bar potential. The distribution of the dust in the bar of NGC 1530 is much narrower than the distribution in NGC 2903. In NGC 1530, the dust lanes are straight and clearly delineated as opposed to the broken feathery morphology of the dust lanes in NGC 2903 (Fig. 2e). This may indicate that no strong shocks are present in the bar of NGC 2903, in contrast to the large velocity gradients perpendicular to the bar in NGC 1530 (Zurita et al. 2004), suggesting that shocks are driving the observed morphology in NGC 1530.

Streaming motions along the bar of NGC 2903 were detected by Leon et al. (2008) using HCN(1−0) as the kinematic tracer. An ongoing analysis of the velocity gradients in the ionised gas of NGC 2903, using the data published by Hernandez et al. (2005), will clarify whether strong velocity gradients are present or not in the bar of NGC 2903. Therefore, although the NIR emission suggest that NGC 2903 hosts a strong bar, the broken and wide structure of the dust lanes may well be evidence that it does not.

The presence of H II regions in both the trailing and leading sides of the dust lanes in NGC 1530 and an age gradient between both sets of H II regions, provides support to the hypothesis (Sheth et al. 2002) that massive stars form in the trailing side of the bar dust lane and move to the leading side. There are no H II regions on the trailing side of the bar of NGC 2903, and no trend in H II region age is found across the bar. This may indicate that the explanation of where star-formation is favoured, is not as straightforward as in NGC 1530, or at least is not as clearly driven by the strong bar dynamics.

The complexity of the SF properties in the bar of NGC 2903 is also illustrated by the presence of compact UV sources without significant 24 μm and Hα emission. These regions are located symmetrically with respect to the centre of the galaxy and nearly perpendicular to the bar as well as in a spiral pattern. All of these regions have FUV−NUV colours compatible with ages of a couple of hundred Myr. The lack of Hα emission suggests that these locations are currently not encouraged by the bar potential to form stars. These stars might have formed somewhere else in the bar and migrated afterwards to the current position. But then a few questions would arise: (1) where did these stars form?; (2) are the stars that are currently forming likely to remain at similar locations?; or, (3) in contrast, were they formed during a more general SF burst possibly linked to the bar formation, or a merger? An ongoing analysis of both the H I and Hα velocity fields will shed some light onto the origin of the UV complexes.

The *current* SFR in the bar, as calculated from Hα, is similar to those of other disk galaxies, although the bar contains a considerably high amount of dense cold gas, as traced by the HCN(1−0) (Leon et al. 2008). The *recent* SFR, as calculated from UV emission, is compatible with that of the *current* SFR.

We draw attention to the offsets of a few arcseconds between the emission peaks in the 24 μm and the *GALEX* images. The 24 μm emission is a good tracer of current star-formation, while UV emission is a "time-averaged" recent star-formation indicator (e.g.; Calzetti et al. 2005). The offsets found here (also seen in M 51 by Calzetti et al. 2005) indicate an evolutionary link between the sites where current star-formation is occurring and the position of the UV counterpart. Estimations of the rotation curve and the pattern speed would be necessary to determine whether the dynamical timescales are compatible with the ageing of the regions.

7. Summary and conclusions

We have performed a detailed multiwavelength study of observations from UV to sub-millimeter wavelengths of the NGC 2903 bar and its surrounding regions. We have mapped and catalogued the H II regions of the bar and measured their Hα equivalent widths. Furthermore, we have obtained a catalogue of the UV emitting regions, and measured their peak locations with respect to those in the Hα image. The extinction has been estimated using the Hα and 24 μm emission. Values of SFRs using both Hα and UV indicators have been calculated. We have estimated the age of the regions, using the $EW_{H\alpha}$ and the FUV$-$NUV colour together with stellar population synthesis models. Our main results are:

– NGC 2903 is a morphologically complex galaxy. Both the near-infrared and the CO ($J = 1-0$) band images detect a clear barred structure, whereas the Hα and UV maps show a patchy spiral-like structure.
– There are clear spiral-like UV complexes with no significant Hα, 24 μm, and CO ($J = 1-0$) counterpart emission. These complexes are located northwest and Southeast of the bar within the inner 1 arcminute radius (corresponding to ~2.5 kpc).
– The Hα emission along the bar, leads the CO. The 3.6 μm and CO ($J = 1-0$) emission trace each other, both leading the major axis of the optical light distribution.
– The Hα luminosities and $EW_{H\alpha}$ of the bar H II regions are within typical ranges for H II regions in both bar and unbarred spirals. The spatial distribution of the Hα EWs does not correlate with any morphological feature in the bar.
– The average dust attenuation in the bar area of NGC 2903 is $A_{H\alpha} = 1.06$, and ranges from 0 to 1.5 mag.
– The FUV$-$NUV colour distribution is distributed into two regions. The bluer regions range from -0.18 to 0.15 implying an age between ~3 and 10 Myr. The redder regions have colours ranging from 0.4 to 0.85, which imply ages ranging from 150 to 400 Myr. The latter correspond to regions with significant amounts of neither Hα nor 24 μm emission.
– The SFRs of the bar region derived from both Hα and the UV emission are $0.9 \pm 0.2\ M_\odot\ \mathrm{yr}^{-1}$ and $0.4 \pm 0.1\ M_\odot\ \mathrm{yr}^{-1}$, respectively.

All these results suggest that some process triggered a SF burst a few hundred Myrs ago. Interestingly, we do detect some stellar clusters unrelated to the current SF locations, symmetrically located nearly perpendicular to the bar (in the inner ~2.5 kpc). These regions might originate from this SF burst.

In a future paper, we will analyse the gas kinematics of the galaxy, with the aim of shedding some light on the origin (merger versus secular evolution) of these findings.

References

Alonso-Herrero, A., Ryder, S. D., & Knapen, J. H. 2001, MNRAS, 322, 757
Athanassoula, E. 1992, MNRAS, 259, 345
Bianchi, L., & Efremova, B. V. 2006, AJ, 132, 378
Bianchi, L., Madore, B., Thilker, D., Gil de Paz, A., & GALEX Science Team 2003, in BAAS, 35, 1354
Bianchi, L., Thilker, D. A., Burgarella, D., et al. 2005, ApJ, 619, L71
Bresolin, F., & Kennicutt, Jr., R. C. 1997, AJ, 113, 975
Calzetti, D. 2001, PASP, 113, 1449
Calzetti, D., Armus, L., Bohlin, R. C., et al. 2000, ApJ, 533, 682
Calzetti, D., Kennicutt, Jr., R. C., Bianchi, L., et al. 2005, ApJ, 633, 871
Cedrés, B., Cepa, J., & Tomita, A. 2005, ApJ, 634, 1043
Dale, D. A., Cohen, S. A., Johnson, L. C., et al. 2009, ApJ, 703, 517
Drozdovsky, I. O., & Karachentsev, I. D. 2000, A&AS, 142, 425
Engelbracht, C. W., Blaylock, M., Su, K. Y. L., et al. 2007, PASP, 119, 994
Fazio, G. G., Hora, J. L., Allen, L. E., et al. 2004, ApJS, 154, 10
Gonzalez Delgado, R. M., & Perez, E. 1997, ApJS, 108, 199
Gordon, K. D., Rieke, G. H., Engelbracht, C. W., et al. 2005, PASP, 117, 503
Gordon, K. D., Engelbracht, C. W., Rieke, G. H., et al. 2008, ApJ, 682, 336
Helfer, T. T., Thornley, M. D., Regan, M. W., et al. 2003, ApJS, 145, 259
Hernandez, O., Carignan, C., Amram, P., Chemin, L., & Daigle, O. 2005, MNRAS, 360, 1201
Hibbard, J. E., Bianchi, L., Thilker, D. A., et al. 2005, ApJ, 619, L87
Iglesias-Páramo, J., Buat, V., Takeuchi, T. T., et al. 2006, ApJS, 164, 38
Irwin, J. A., Hoffman, G. L., Spekkens, K., et al. 2009, ApJ, 692, 1447
Kennicutt, Jr., R. C. 1983, ApJ, 272, 54
Kennicutt, Jr., R. C. 1998, ARA&A, 36, 189
Kennicutt, Jr., R. C., & Kent, S. M. 1983, AJ, 88, 1094
Kennicutt, Jr., R. C., Edgar, B. K., & Hodge, P. W. 1989, ApJ, 337, 761
Kennicutt, Jr., R. C., Armus, L., Bendo, G., et al. 2003, PASP, 115, 928
Kennicutt, Jr., R. C., Calzetti, D., Walter, F., et al. 2007, ApJ, 671, 333
Kennicutt, R. C., Hao, C., Calzetti, D., et al. 2009, ApJ, 703, 1672
Kong, X., Charlot, S., Brinchmann, J., & Fall, S. M. 2004, MNRAS, 349, 769
Koribalski, B. S., & López-Sánchez, Á. R. 2009, MNRAS, 400, 1749
Kormendy, J. 1979, ApJ, 227, 714
Kuchinski, L. E., Freedman, W. L., Madore, B. F., et al. 2000, ApJS, 131, 441
Laurikainen, E., & Salo, H. 2002, MNRAS, 337, 1118
Lee, J. C., Kennicutt, R. C., Engelbracht, C. W., et al. 2008, in ed. J. G. Funes, & E. M. Corsini, ASP Conf. Ser., 396, 151
Lee, J. C., Gil de Paz, A., Tremonti, C., et al. 2009, ApJ, 706, 599
Leitherer, C., Schaerer, D., Goldader, J. D., et al. 1999, ApJS, 123, 3
Leon, S., Jeyakumar, S., Pérez-Ramírez, D., et al. 2008, A&A, 491, 703
Martin, P., & Friedli, D. 1997, A&A, 326, 449
Martin, D. C., Fanson, J., Schiminovich, D., et al. 2005, ApJ, 619, L1
Mayya, Y. D. 1994, AJ, 108, 1276
Pérez, I., Fux, R., & Freeman, K. 2004, A&A, 424, 799
Pérez-González, P. G., Kennicutt, Jr., R. C., Gordon, K. D., et al. 2006, ApJ, 648, 987
Pilyugin, L. S., Vílchez, J. M., & Contini, T. 2004, A&A, 425, 849
Regan, M. W., Thornley, M. D., Helfer, T. T., et al. 2001, ApJ, 561, 218
Relaño, M., & Kennicutt, R. C. 2009, ApJ, 699, 1125
Relaño, M., Beckman, J. E., Zurita, A., Rozas, M., & Giammanco, C. 2005, A&A, 431, 235
Rieke, G. H., Young, E. T., Engelbracht, C. W., et al. 2004, ApJS, 154, 25
Rozas, M., Zurita, A., Heller, C. H., & Beckman, J. E. 1999, A&AS, 135, 145
Salim, S., Rich, R. M., Charlot, S., et al. 2007, ApJS, 173, 267
Schlegel, D. J., Finkbeiner, D. P., & Davis, M. 1998, ApJ, 500, 525
Scoville, N. Z., Polletta, M., Ewald, S., et al. 2001, AJ, 122, 3017
Sheth, K., Vogel, S. N., Regan, M. W., et al. 2002, AJ, 124, 2581
Tamura, K., Jansen, R. A., & Windhorst, R. A. 2009, AJ, 138, 1634
Thilker, D. A., Bianchi, L., Boissier, S., et al. 2005, ApJ, 619, L79
Thilker, D. A., Boissier, S., Bianchi, L., et al. 2007, ApJS, 173, 572
Verley, S., Corbelli, E., Giovanardi, C., & Hunt, L. K. 2009, A&A, 493, 453
von Hippel, T., & Bothun, G. 1990, AJ, 100, 403
Werner, M. W., Roellig, T. L., Low, F. J., et al. 2004, ApJS, 154, 1
Zurita, A., & Pérez, I. 2008, A&A, 485, 5
Zurita, A., Relaño, M., Beckman, J. E., & Knapen, J. H. 2004, A&A, 413, 73